

All-dielectric metasurface-coupled quantum well infrared photodetectors with enhanced responsivity

Xin Rui^{1,2}, Xia Hui^{1,2}, Qiao Liang^{1,3}, Xia Peng-Zhe^{1,3}, Chen Zhen^{1,4}, Yao Shu-Fan^{1,4}, Lu Wei¹, Li Tian-Xin^{1,2*}

- (1. State Key Laboratory of Infrared Physics, Shanghai Institute of Technical Physics, Chinese Academy of Sciences, Shanghai 200083, China;
2. University of Chinese Academy of Sciences, Beijing 100049, China;
3. School of Physical Science and Technology, ShanghaiTech University, Shanghai 201210, China;
4. School of Microelectronics, Shanghai University, Shanghai 201899, China)

Abstract: Quantum well infrared photodetectors (QWIPs) are widely utilized in long-wave infrared (LWIR) detection applications, yet they are constrained by low quantum efficiency (QE). Although metallic microcavities can enhance local coupling, achieving a field strength that perfectly coincides with the quantum well (QW) layers remains challenging, and such approaches are often incompatible with thick active regions. In this study, we developed an all-dielectric metasurface-coupled QWIP (MS-QWIP) to enhance device response. The metasurface features a square micropillar array etched directly into the 80-period GaAs/AlGaAs multi-quantum wells (MQWs) active region. By leveraging the guided-mode resonance (GMR) effect, this structure excites a strong longitudinal electric field component (E_z), effectively satisfying the ISBT selection rule for enhanced absorption within the active region. Experimental results at 50 K and a 5 V bias show that the peak responsivity of the MS-QWIP reaches 545 mA/W, a twofold increase over a conventional 45° facet-coupled device. Furthermore, the blackbody responsivity is improved by approximately 1.6 times. Notably, the architecture also reduces the effective electrical area of the photosensitive element, thereby suppressing dark current. This work demonstrates that all-dielectric metasurfaces can significantly enhance the sensitivity and signal-to-noise ratio of QWIPs.

Key words: quantum wells, semiconductor detector, long-wave infrared, dielectric metasurface

PACS:

Introduction

Infrared detection technology constitutes a cornerstone of modern optoelectronics, serving as an indispensable tool across a vast spectrum of critical applications, such as military reconnaissance, space-borne remote sensing, non-destructive industrial testing, and high-resolution medical imaging^[1-3]. In this technical field, quantum well infrared photodetectors (QWIPs) have garnered significant attention due to the mature GaAs/AlGaAs material growth technology, which enables the fabrication of large-area focal plane arrays (FPAs) with high spatial uniformity, particularly within the long-wave infrared (LWIR) atmospheric window^[4-6]. However, despite these advantages, QWIPs are constrained by a fundamental physical bottleneck imposed by the intersubband transition (ISBT) selection rule. In conventional n-type quantum well (QW) structures, optical absorption is strictly limited to incident light with an electric field com-

ponent perpendicular to the QW plane (z-polarization)^[7]. This inherent polarization dependence inevitably results in relatively low quantum efficiency and responsivity.

To overcome these limitations and achieve high-performance infrared detection, researchers have developed a variety of optical coupling enhancement structures, such as Brewster-angle facet coupling^[8] and metal microcavity architectures^[9], all dedicated to facilitating efficient infrared absorption. Metal plasmonic microstructures^[10-12] and metamaterials^[13-14] are regarded as ideal candidates for achieving effective coupling with subwavelength spatial modes and enhancing localized electric fields. For instance, Chen et al. developed an infrared detector integrated with metallic nanoantenna arrays, which can harvest photons from an area significantly larger than the physical footprint of device and confine the electromagnetic field into subwavelength microcavities to

Foundation items: Supported by the Chinese Academy of Sciences (XDB0580000, GJ0090406), the National Natural Science Foundation of China (12393833, 12227901, U2241219, 12174416, 11991063), and the Science and Technology Commission of Shanghai Municipality (23JC1404100)

Biography: Xin Rui (1998-), female. Research area involves quantum well infrared photodetectors. E-mail: xr41721162@163.com

* **Corresponding author:** E-mail: txli@mail. sip. ac. cn

boost responsivity^[15]. Furthermore, Miyazaki et al. demonstrated an external quantum efficiency (EQE) of 61% at 78 K by employing optimized folded-line antennas coupled with a single QW^[16]. Despite the superior optical performance of metallic coupling structures, they are often hindered by significant intrinsic Ohmic losses. More importantly, their efficacy is fundamentally restricted to shallow active layers due to the limited penetration depth of surface plasmon polaritons (SPPs)^[17-18]. For devices requiring thick active regions to ensure sufficient absorption, metallic metasurfaces typically fail to propagate the resonant field throughout the entire MQW active region, leaving the underlying QWs unable to absorb light^[19]. To mitigate these drawbacks, dielectric optical coupling structures have emerged as a compelling alternative^[20-21]. Unlike metallic microcavities, dielectric architectures primarily leverage the guided-mode resonance (GMR) effect to confine infrared radiation within the dielectric media^[22-23]. Such structures not only excite robust longitudinal electric field components to satisfy the ISBT selection rule, but also substantially extend the effective optical path length, leading to a marked enhancement in absorption efficiency.

In this work, we developed an all-dielectric metasurface-coupled QWIPs (MS-QWIPs) to overcome the efficiency limits imposed by the ISBT selection rule. By etching a square micropillar array using QW material, we leveraged the guided-mode resonance effect to induce a strong longitudinal electric field (E_z). This architecture significantly enhances optical absorption, achieving a two-fold increase in peak responsivity compared to conventional 45° facet-coupled devices. This approach provides a pathway for the development of high-sensitivity, metasurface-enhanced infrared focal plane arrays.

1 Results and discussions

1.1 Characterization of material properties

The epitaxial material for the all-dielectric metasurface QW device consists of an 80-period multi-quantum wells (MQWs) structure. Each period comprises a 5.4 nm GaAs well and a 40 nm $\text{Al}_{0.26}\text{Ga}_{0.74}\text{As}$ barrier. The central 2 nm of each GaAs well is Si-doped with a designed carrier concentration of $3.5 \times 10^{18} \text{ cm}^{-3}$. This MQWs active region is sandwiched between two n+

doped GaAs contact layers that the top and bottom contact layers have thicknesses of 0.95 μm and 1.1 μm , respectively. Both contact layers maintain at a doping level of $1.0 \times 10^{18} \text{ cm}^{-3}$.

To verify the growth quality and energy level distribution of the QW material, the photoluminescence (PL) spectrum of the sample was measured at room temperature (300 K), as shown in Fig. 1(a). Two prominent characteristic peaks are clearly observed in the spectrum. The primary peak at 815.3 nm (1.53 eV) corresponds to the electron-hole recombination radiation within the GaAs well layer. Meanwhile, the secondary peak at 708.7 nm (1.75 eV) corresponds to the emission signal from the AlGaAs barrier layer. The relationship between the bandgap energy E_g of AlGaAs, the Al composition x , and the temperature T is defined by the following equation^[24]: $E_g(\text{AlGaAs}) = 1.519 + 1.247x - 0.0005405T^2 / (T + 204)$. By utilizing the PL peak position, the Al composition x was calculated to be 0.262. This result is in good agreement with the original design specifications.

Based on the Al composition of 0.262 determined from the PL characterization, the band structure and the corresponding subband energies of the QW material was calculated. Fig. 1(b) illustrates the energy level structure of a single QW, clearly marking the ground state level (E_0), the first excited state level (E_1), and their respective wavefunction distributions. Notably, lies significantly below the barrier edge, indicating that the inter-subband transition in this QW is a bound-to-bound (B-B) transition^[25]. The transition energy is calculated as: $\Delta E = E_1 - E_0 = 0.155 \text{ eV}$, which corresponds to a theoretical response wavelength of approximately 8 μm . Fig. 1(c) presents the intrinsic photoresponse of the 45° device, revealing a peak response wavelength of 8.1 μm , which is in excellent agreement with the theoretical calculations. However, the blackbody responsivity is only 30 mA/W at 5 V. The high doping level intended in the design did not yield the expected high responsivity.

To investigate the electrical properties of QW material, we employed scanning spreading resistance microscopy (SSRM) to determine the actual carrier concentration within the QW (as shown in Fig. 2). Fig. 2(a) presents a cross-section SSRM resistance distribution map for the QWs sample. Alternating dark and light

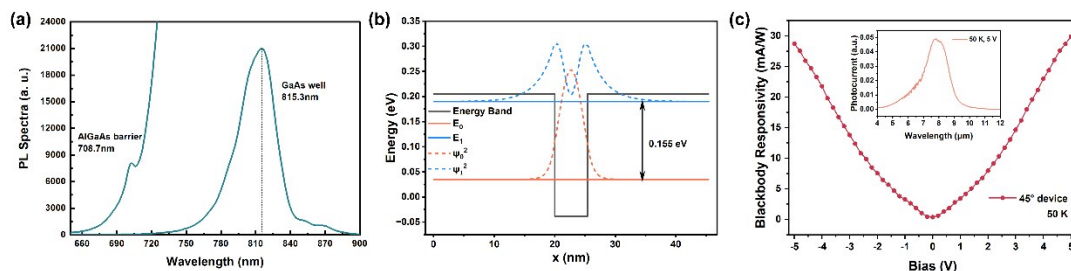


Fig. 1 Material characteristics and photoelectric performance of the MQWs device: (a) PL spectrum of the MQWs material at 300 K; (b) Energy level structure of the 80-QWs sample; (c) Blackbody responsivity of the 45° device, with the inset displaying the corresponding photocurrent spectrum

图1 多量子阱器件的材料特性与光电性能:(a)300 K下多量子阱(MQWs)材料的光致发光(PL)光谱;(b)80-QWs样品的能级结构图;(c)45°器件的黑体响应率,插图显示了相应的光电流光谱

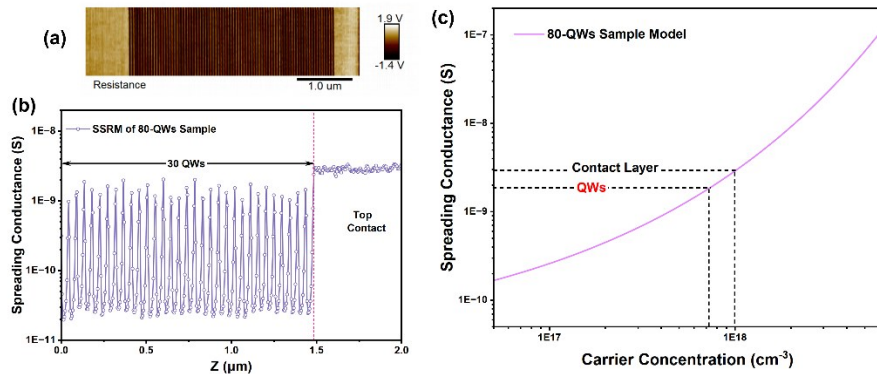


Fig. 2 Cross-sectional electrical characterization of the 80-QWs sample using SSRM: (a) Cross-sectional SSRM image of the 80-QWs sample; (b) Spreading conductance extracted along the growth direction of the 80-QWs sample; (c) Numerical simulation results of the relationship between carrier concentration and tip-sample spreading conductance for the contact layer and QWs.

图2 80周期量子阱样品的SSRM表征:(a)80-QWs样品的截面SSRM图像;(b)沿80-QWs样品生长方向提取的分布电导;(c)接触层与QWs的载流子浓度与探针-样品分布电导之间关系的数值模拟结果

stripes are observed in the image, corresponding to the periodic arrangement of the well and barrier layers. This contrast reflects significant differences in local resistance between the various epitaxial layers due to different doping levels. As shown in Fig. 2(b), the spreading conductance distribution curve extracted along the growth direction of the material encompasses 30 periods of the QWs and a portion of the upper electrode layer. The electron concentration within the QW were calculated from measured conductance using the quantitative model established in Ref. [26]. According to the relationship between carrier concentration and tip-sample conductance shown in Fig. 2(c), the actual electron concentration in the QW was found to be only $7.3 \times 10^{17} \text{ cm}^{-3}$, which is lower than the design specification of $3.5 \times 10^{18} \text{ cm}^{-3}$. This significantly low electron concentration is responsible for the poor responsivity of the material.

1.2 Fabrication and Performance Characterization of All-Dielectric Metasurface QWIP

To enhance device performance, we introduced an all-dielectric metasurface entirely composed of the QW material. As illustrated in Fig. 3(a), the metasurface

consists of a periodic array of square micropillars defined by height (h), size (a), and period (P). To facilitate electrical readout across the micropillars, adjacent micropillars are interconnected by 300-nm-wide wires made of the same material. These square micropillars are fabricated via etching process through the epitaxial layers, the details of which are depicted in the right panel of Fig. 3(a). This all-dielectric structure functions simultaneously as the absorption medium and the coupling grating, which can excite GMR effect^[27]. This dual functionality effectively addresses the inherent limitation of QWIPs by generating a significant z-direction electric field (E_z) component, which directly satisfies the selection rules for ISBT absorption.

The optical performance of the metasurface was evaluated using the Finite-Difference Time-Domain (FDTD) method^[28]. Fig. 3(b) illustrates the simulated transmission, reflection, and absorption spectra for the geometry as $a = 1.8 \mu\text{m}$, $P = 4.5 \mu\text{m}$ and $h = 4.5 \mu\text{m}$. A distinct reflection minimum is observed near $8 \mu\text{m}$, signifying an excellent impedance match and an effective anti-reflection property. Simultaneously, the transmission spec-

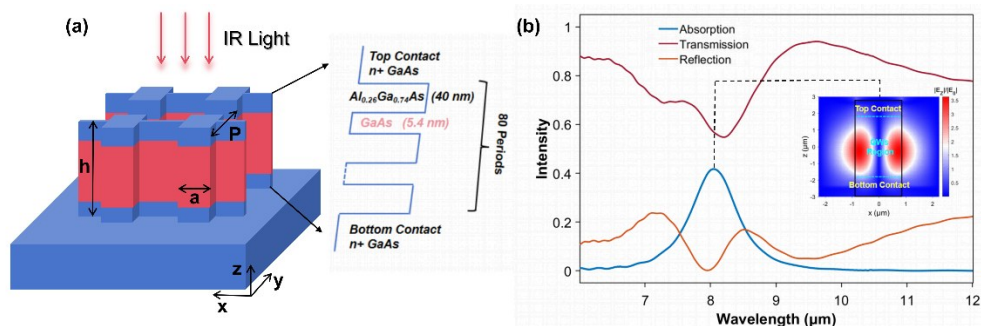


Fig. 3 Schematic illustration of the square micropillar metasurface structure and its simulated optical performance: (a) Schematic of the square micropillar dielectric metasurface structure. The epitaxial layer details are shown on the right, consisting of 80 periods of $\text{Al}_{0.26}\text{Ga}_{0.74}\text{As}/\text{GaAs}$ QWs; (b) Simulated transmission (red line), reflection (orange line), and absorption (blue line) spectra. The inset illustrates the z-direction electric field (E_z) distribution in the x-z plane at the peak absorption wavelength

图3 方形微柱超表面结构示意图及其模拟光学性能:(a)正方形微柱介质超表面结构的示意图。右侧展示了外延层的详细信息,该层由80个周期的 $\text{Al}_{0.26}\text{Ga}_{0.74}\text{As}/\text{GaAs}$ QWs组成;(b)模拟的透射光谱(红线)、反射光谱(橙线)和吸收光谱(蓝线)。插图展示了在峰值吸收波长处,x-z平面内的z方向电场(E_z)分布图

trum exhibits a corresponding dip, suggesting that the incident radiation is neither reflected nor directly transmitted. Instead, the incident light is efficiently coupled into the dielectric micropillars. In this mechanism, the periodic all-dielectric structure functions simultaneously as an absorption medium and a subwavelength coupling grating, establishing an excellent impedance match with the incident waves. Under this resonant condition, the infrared radiation is strongly confined and subsequently absorbed by the MQWs region, resulting in an absorption peak at $8.1 \mu\text{m}$. The relatively large pillar height ($h = 4.5 \mu\text{m}$) facilitates deep evanescent coupling and increases the interaction volume, yielding a peak absorption intensity as high as 0.4. The inset of Fig. 3(b) depicts the E_z field distribution in the x - z plane at the resonance wavelength. In the x -direction, the electric field intensity gradually decays from the center of the micropillar toward the edges, exhibiting the characteristic distribution of a fundamental mode (HE_{11})^[29]. Furthermore, the high-intensity E_z region extensively permeates the entire $3.67 \mu\text{m}$ -thick active region, effectively overcoming the polarization limitations by directly satisfying the ISBT selection rule. This achieves an ideal spatial overlap between the resonant mode and the 80-period MQW stack, ensuring that the enhanced field is fully utilized across the entire absorption volume. Such deep-volume coupling dramatically strengthens light-matter interaction, thereby significantly improving the overall absorption efficiency of the QWs.

ciency of the QWs.

The geometric parameters of the micropillars, specifically the size (a) and the array period (P), are critical factors governing the absorption intensity. To determine the optimal configuration, FDTD simulations were performed with the pillar height fixed at $4.5 \mu\text{m}$. As shown in Fig. 4(a), the absorption evolution is investigated as a function of size (a). Within the range of $1.0 \mu\text{m}$ to $2.4 \mu\text{m}$, the absorption exhibits a trend of initially increasing and subsequently decreasing. When size (a) falls between $1.6 \mu\text{m}$ and $1.8 \mu\text{m}$, the structure achieves optimal impedance matching with the incident waves, resulting in maximum absorption intensity (indicated by the dark blue region). Fig. 4(b) illustrates the influence of the period P on the absorption spectrum. Compared to the size (a), the period (P) exerts a relatively weak modulation effect on the central absorption wavelength, which remains consistently around $8 \mu\text{m}$. The maximum absorption is realized when the structural resonance wavelength precisely aligns with the intrinsic absorption of the quantum well material. Consequently, for QWs materials with a peak response wavelength of $8 \mu\text{m}$, the optimal geometric dimensions are identified as $a = 1.8 \mu\text{m}$ and $P = 4.5 \mu\text{m}$.

All-dielectric metasurface-coupled QWIPs (MS-QWIPs) were successfully fabricated using electron beam lithography (EBL) combined with inductively coupled plasma reactive ion etching (ICP-RIE). During the

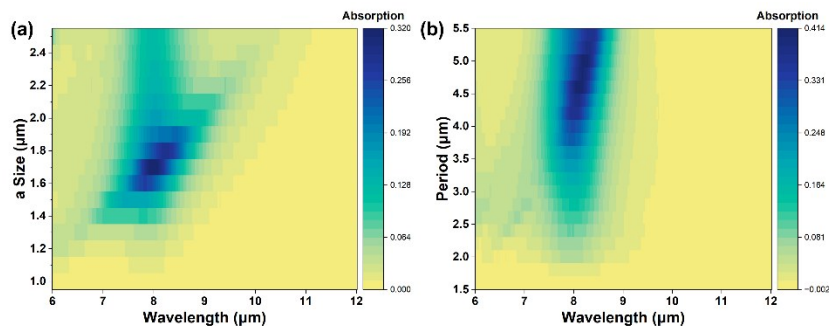


Fig. 4 Simulated absorption spectra of the MS-QWIPs: (a) Spectra with varying micropillar sizes a ; (b) Spectra with varying array periods P

图4 MS-QWIPs 的模拟吸收光谱:(a)改变微柱尺寸 a 的光谱;(b)改变阵列周期 P 的光谱

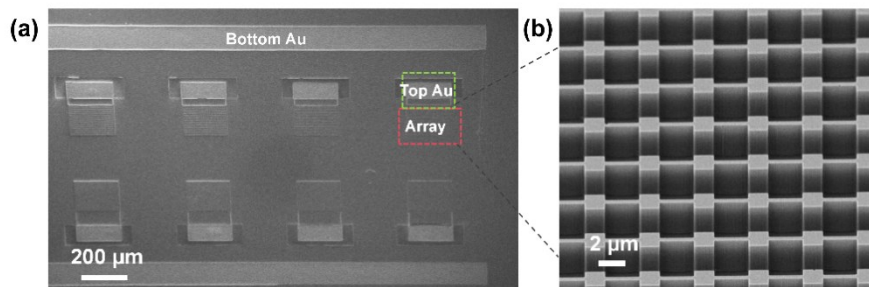


Fig. 5 SEM characterization of the MS-QWIPs: (a) Scanning electron microscopy (SEM) image of the dielectric MS-QWIP device array; (b) SEM image of the square micropillar dielectric metasurface array by ICP-RIE etching

图5 MS-QWIPs 的 SEM 表征:(a)MS-QWIP 器件阵列的扫描电子显微镜(SEM)图像;(b)通过 ICP-RIE 刻蚀制备的正方形微柱介质超表面阵列的 SEM 图像

ICP-RIE process, a fraction of N_2 (approximately 9.1%) was introduced into the $Cl_2/BCl_3/Ar$ gas mixture. This N_2 -assisted etching chemistry promotes the formation of a dense, protective passivation layer on the etched sidewalls^[30]. This layer acts as a robust barrier that prevents lateral chemical etching, which is crucial for maintaining the structural of the MQW active region after etching. Fig. 5 (a) presents the scanning electron microscopy (SEM) image of the completed MS-QWIP array. The array consists of 4×2 independent device units with different geometric parameters of the micropillars, where the top electrodes (Top Au), bottom electrodes (Bottom Au), and the core metasurface array regions (Array) are clearly discernible. Fig. 5(b) provides a high-magnification SEM view of the micropillars region. The micropillars exhibit superior morphological characteristics, featuring smooth sidewalls, excellent verticality, and highly uniform etching depth. Such high-quality structural integrity provides a robust physical foundation for achieving efficient electromagnetic coupling.

Under the regulation of the all-dielectric metasurface, the photoelectric performance of the QWIP devices exhibits significant optimization, primarily manifested in

the enhancement of responsivity. To verify the structural efficacy in improving light coupling efficiency, blackbody responsivity measurements were performed using a 500 K blackbody as the thermal radiation source at an operating temperature of 50 K. Fig. 6 (a) illustrates the blackbody responsivity of devices with varying micropillar sizes (a) (at a fixed period $P = 4.5 \mu\text{m}$). The responsivity of all devices increases with the bias voltage. Notably, the device achieves its peak response at $a = 1.8 \mu\text{m}$, which is attributed to the optimal matching between the GMR excited by the micropillars and the incident wavelength at this specific dimension. Fig. 6 (b) compares the blackbody responsivity of the MS-QWIP (with $a = 1.8 \mu\text{m}$ and $P = 4.5 \mu\text{m}$) against a 45° facet-coupled device. The results demonstrate that the MS-QWIP consistently outperforms the 45° device across the entire bias range. At a 5 V bias, the blackbody responsivity of the MS-QWIP reaches approximately 54.2 mA/W, whereas the 45° device yields only 33.8 mA/W. As shown in the inset of Fig. 6(b), the responsivity of the MS-QWIP is enhanced by approximately 1.6 times compared to the 45° device, underscoring the superior light-coupling capabilities of the integrated metasurface.

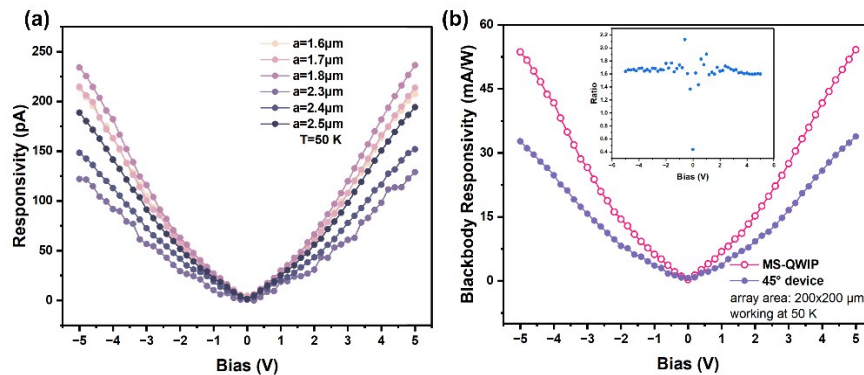


Fig. 6 Blackbody responsivity of the MS-QWIPs: (a) Responsivity of micropillar structures with various a size under a 500 K blackbody source; (b) Comparison of blackbody responsivity between the MS-QWIP ($a=1.8 \mu\text{m}$, $P=4.6 \mu\text{m}$) and the 45° device. The inset shows the responsivity ratio

图6 MS-QWIPs的黑体响应率:(a)在500 K黑体辐射源照射下,不同尺寸 a 的微柱结构的响应率;(b)MS-QWIP($a=1.8 \mu\text{m}$, $P=4.6 \mu\text{m}$)与 45° 器件的黑体响应率对比。插图展示了两者的响应率的比值(增强倍数)

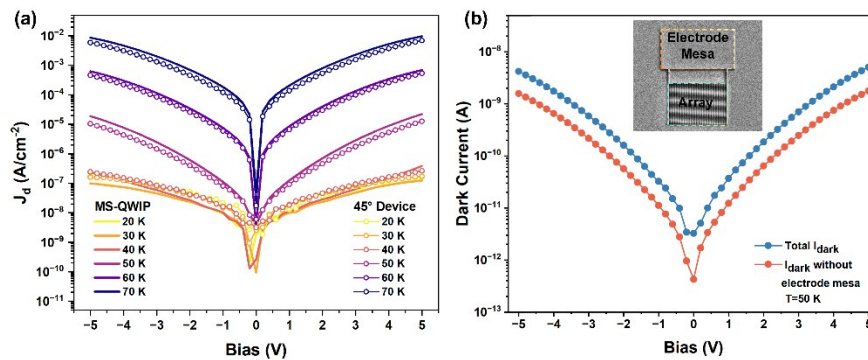


Fig. 7 Dark current characteristics of the MS-QWIPs: (a) Comparison of dark current density (J_d) between MS-QWIP and 45° device at different temperatures; (b) Comparison of dark current curves for devices with and without the contribution of the electrode mesa at 50 K. The inset shows an SEM image of the device

图7 MS-QWIPs的暗电流特性:(a)MS-QWIP与 45° 器件在不同温度下的暗电流密度(J_d)对比图;(b)在50 K下包含与不包含电极台面贡献的器件暗电流曲线对比。插图展示了该器件的SEM图像

Fig. 7(a) compares the dark current densities (J_d) of the MS-QWIP and the 45° device at different temperatures. The results indicate that both devices exhibit nearly identical dark current density. Remarkably, while the deep etching process increased the total sidewall surface area of the MS-QWIP by approximately 30 times compared to the 45° device, no significant increase in J_d was observed. This provides compelling evidence for the high quality of the micropillar array etching process. Specifically, the N_2 -promoted passivation effectively terminates dangling bonds and seals the exposed sidewalls, thereby preventing the formation of surface-state-induced leakage channels^[30]. Fig. 7(b) presents a comparison of dark current curves with and without the contribution from the electrode mesa. The inset SEM image clearly delineates the electrode mesa region and the detector array region. The comparison reveals that the total dark current is significantly higher than the dark current excluding the electrode mesa contribution. Consequently, optimizing the geometry of the electrode mesa or implementing more effective isolation processes is expected to further reduce the dark current of the detector.

Fig. 8(a) shows the photoresponse spectra of the MS-QWIP and the 45° device at 50 K with a bias voltage of 5 V. Both devices exhibit a consistent peak response wavelength of approximately 8 μm . Notably, the peak responsivity of the MS-QWIP reaches approximately 545 mA/W, representing a twofold increase over the 270 mA/W observed for the 45° device.

The dark current-limited detectivity (D_{dark}^*) is a critical metric for evaluating detector sensitivity, determined by the interplay between responsivity and dark current noise, D_{dark}^* can be calculated as^[31]:

$$D_{\text{dark}}^* = \frac{R \sqrt{A}}{\sqrt{4e g_{\text{noise}} I_{\text{dark}}}}, \quad (1)$$

where, g_{noise} represents the noise gain and I_{dark} denotes the dark current of the device. The noise gain is defined as $g_{\text{noise}} = 1/(N_w p_c)$, where N_w is the number of QWs and p_c is the capture probability as 0.1^[7].

Fig. 8(b) displays the D_{dark}^* curves as a function of bias voltage for both the 45° device and the MS-QWIP at 50 K. Although the total dark current of the MS-QWIP is slightly higher due to the inclusion of the electrode mesa, its D_{dark}^* (pink circles) remains superior to that of the 45° device (purple circles) because of the substantial enhancement in responsivity. The D_{dark}^* exceeds 3.0×10^{11} $\text{cmHz}^{1/2}/\text{W}$ across the bias range of 1 V to 5 V. Given that the electrode mesa region contributes significantly to the dark current without aiding the photoresponse, the intrinsic performance of the MS-QWIP (pink stars) was further evaluated by excluding this non-photosensitive area. The result represents an approximately threefold improvement over the standard 45° device, demonstrating that the integration of all-dielectric metasurface can significantly enhance the signal-to-noise ratio of QWIP.

2 Conclusions

In summary, we have successfully demonstrated a high-performance GaAs/AlGaAs QWIP integrated with an all-dielectric metasurface designed for the LWIR regime. By fabricating a square micropillar array consist of the MQW active region, efficient optical coupling was achieved through guided-mode resonance (GMR). FDTD simulations confirmed that the optimized geometric parameters ($a = 1.8 \mu\text{m}$, $P = 4.5 \mu\text{m}$) provide ideal impedance matching, ensuring that the maximum E_z field intensity perfectly overlaps with the active layers to satisfy the intersubband transition selection rule. Consequently, the MS-QWIP reached a peak responsivity of 545 mA/W at 8 μm , representing a two-fold enhancement compared to the traditional 45° facet-coupled device. Crucially, despite a 30-fold increase in sidewall surface area, the MS-QWIP maintained a dark current density comparable to the reference device, validating the high-quality ICP-RIE etching process. This work provides a robust strategy for developing high-sensitivity, metasurface-enhanced infrared focal plane arrays.

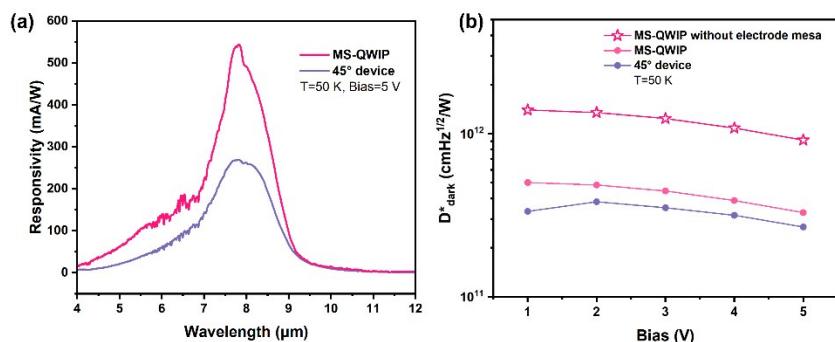


Fig. 8 Spectral responsivity and detectivity of the MS-QWIP: (a) Comparison of responsivity spectra for the 45° device (purple) and the MS-QWIP (pink) at a bias of 5 V and an operating temperature of 50 K; (b) Dark current limited detectivity (D_{dark}^*) as a function of bias voltage at 50 K for the 45° device (purple circles), the MS-QWIP (pink circles), and the intrinsic MS-QWIP performance excluding the electrode mesa area (pink stars)

图8 MS-QWIP的光谱响应率和探测率:(a)在5 V偏压和50 K工作温度下,45°器件(紫色)与MS-QWIP(粉色)的响应率光谱对比;(b)50 K温度下,45°器件(紫色圆点)、MS-QWIP(粉色圆点)以及排除电极台面面积影响后的本征MS-QWIP性能(粉色星形)的暗电流受限探测率(D_{dark}^*)随偏置电压的变化关系图

References

- [1] Tan C L, Mohseni H. Emerging technologies for high performance infrared detectors [J]. *Nanophotonics*, 2018, 7 (1) : 169-197.
- [2] Wang Y, Li J, Sun H, et al. A review on the developments and space applications of mid- and long-wavelength infrared detection technologies [J]. *Frontiers of Information Technology & Electronic Engineering*, 2024, 25(8) : 1031-1056.
- [3] Li Y, Cao B, Su X, et al. Infrared array imaging for precise temperature measurement and temperature compensation [J]. *Infrared and Laser Engineering*, 2024, 53 (10) : 20240269-1-20240269-10.
- [4] Xiangyang L, Ning L, Jintong X, et al. GaAs/AlGaAs QWIP IRFPA for 10.55 μm long wavelength [J]. *Infrared and Laser Engineering*, 2020, 49(1) : 0103008-0103008(6).
- [5] Dely H, Joharifar M, Durupt L, et al. Unipolar quantum optoelectronics for high speed direct modulation and transmission in 8 - 14 μm atmospheric window [J]. *Nature Communications*, 2024, 15(1) : 8040.
- [6] Lu H, Li N, Zhou X, et al. An LWIR QWIP FPA with sub-5mK NETD and large dynamic range [J]. *Infrared Physics & Technology*, 2025, 144 : 105629.
- [7] Schneider H, Liu H C. *Quantum Well Infrared Photodetectors* [M]. Springer, 2006.
- [8] Hinds S, Buchanan M, Dudek R, et al. Near-room-temperature mid-infrared quantum well photodetector [J]. *Advanced Materials*, 2011, 23(46) : 5536-5539.
- [9] Jing Y L, Li Z F, Li Q, et al. Pixel-level plasmonic microcavity infrared photodetector [J]. *Scientific Reports*, 2016, 6 (1) : 25849.
- [10] Palaferri D, Todorov Y, Bigioli A, et al. Room-temperature nine- μm -wavelength photodetectors and GHz-frequency heterodyne receivers [J]. *Nature*, 2018, 556(7699) : 85-88.
- [11] Jing W, Deng J, Zhu T, et al. Monolithic High-Accuracy Long-Wave Infrared Full-Stokes Polarimeter Based on a Meta-QWIP [J]. *Laser & Photonics Reviews*, 2026, 20(2) : e01411.
- [12] Yang K, Yao X, Liu B, et al. Metallic Plasmonic Array Structures: Principles, Fabrications, Properties, and Applications [J]. *Advanced Materials*, 2021, 33(50) : 2007988.
- [13] Deng K, Guo J, Zhang K, et al. All-Silicon Broadband Infrared Photodetectors With In-Plane Photon Trapping Structures [J]. *Advanced Materials*, 2025, 37(17) : 2419382.
- [14] Zheng C-L, Ni P-N, Xie Y-Y, et al. On-chip light control of semiconductor optoelectronic devices using integrated metasurfaces [J]. *Opto-Electronic Advances*, 2025, 8 (1) : 240159-1-240159-26.
- [15] Nga Chen Y, Todorov Y, Askenazi B, et al. Antenna-coupled microcavities for enhanced infrared photo-detection [J]. *Applied Physics Letters*, 2014, 104(3) : 031113.
- [16] Miyazaki H T, Mano T, Kasaya T, et al. Synchronously wired infrared antennas for resonant single-quantum-well photodetection up to room temperature [J]. *Nature Communications*, 2020, 11(1) : 565.
- [17] Ding K, Ning C Z. Fabrication challenges of electrical injection metallic cavity semiconductor nanolasers [J]. *Semiconductor Science and Technology*, 2013, 28(12) : 124002.
- [18] Barnes W L, Dereux A, Ebbesen T W. Surface plasmon sub-wavelength optics [J]. *Nature*, 2003, 424(6950) : 824-830.
- [19] Willets K A, Van Duyne R P. Localized Surface Plasmon Resonance Spectroscopy and Sensing [J]. *Annual Review of Physical Chemistry*, 2007, 58 : 267-297.
- [20] Kuznetsov A I, Miroshnichenko A E, Brongersma M L, et al. Optically resonant dielectric nanostructures [J]. *Science*, 2016, 354(6314).
- [21] Aigner A, Weber T, Wester A, et al. Continuous spectral and coupling-strength encoding with dual-gradient metasurfaces [J]. *Nat Nanotechnol*, 2024, 19(12) : 1804-1812.
- [22] Zhang X, You T, Zhao J, et al. Guided-mode-resonant grating-coupled quantum well infrared photodetector for filter-free CH_4 detection [J]. *Physica Scripta*, 2026, 101(2) : 025510.
- [23] Kamboj A, Nordin L, Petluru P, et al. All-epitaxial guided-mode resonance mid-wave infrared detectors [J]. *Applied Physics Letters*, 2021, 118(20) : 201102.
- [24] Wang Y, Yoon S F, Liu C Y, et al. Temperature and excitation density dependent photoluminescence of sputtering-induced GaAs/AlGaAs quantum dots [J]. *Nanotechnology*, 2008, 19 (1) : 015602.
- [25] Gunapala S D, Bandara S V, Rafol S B, et al. Chapter 2-Quantum Well Infrared Photodetectors [M]. Elsevier, 2011, 84 : 59-151.
- [26] Xin R, Li N, Xia H, et al. Probing Electron Density in Quantum Wells and its Impact on the Performance of Infrared Photodetectors [J]. *IEEE Electron Device Letters*, 2024, 45 (10) : 1740-1743.
- [27] Tang W, Zhou J, Zheng Y, et al. All-dielectric resonant waveguide based quantum well infrared photodetectors for hyperspectral detection [J]. *Optics Communications*, 2018, 427 : 196-201.
- [28] Seo D-J, Kyoung J. Shape dependence of all-dielectric terahertz metasurface [J]. *Optics Express*, 2022, 30(21) : 38564-38575.
- [29] Xin-Yang J, Wei-Wei L, Tian-Xin L, et al. Enhanced absorption of infrared light for quantum wells in coupled pillar-cavity arrays [J]. *Optics Express*, 2023, 31(5) : 7090-7102.
- [30] Volatier M, Duchesne D, Morandotti R, et al. Extremely high aspect ratio GaAs and GaAs/AlGaAs nanowaveguides fabricated using chlorine ICP etching with N_2 -promoted passivation [J]. *Nanotechnology*, 2010, 21(13) : 134014.
- [31] Hainey M F, Mano T, Kasaya T, et al. Systematic studies for improving device performance of quantum well infrared stripe photodetectors [J]. *Nanophotonics*, 2020, 9(10) : 3373-3384.

响应度增强的全介质超表面耦合量子阱红外探测器

辛蕊^{1,2}, 夏辉^{1,2}, 乔亮^{1,3}, 夏鹏哲^{1,3}, 陈珍^{1,4}, 姚书凡^{1,4}, 陆卫¹, 李天信^{1,2*}

(1. 中国科学院上海技术物理研究所 红外科学与技术全国重点实验室, 上海 200083;

2. 中国科学院大学, 北京 100049;

3. 上海科技大学 物质科学与技术学院, 上海 201210;

4. 上海大学 微电子学院, 上海 201899)

摘要:量子阱红外探测器(QWIP)广泛应用于长波红外(LWIR)探测领域,但仍受限于较低的量子效率(QE)。虽然金属微腔能够增强局部耦合,但实现与量子阱(QW)层高度完全匹配的场强分布仍面临挑战,且此类方法通常难以兼容厚有源区结构。为了克服这些限制并提高器件响应,开发了一种全介质超表面耦合量子阱红外探测器(MS-QWIP)。该超表面采用干法刻蚀将80周期GaAs/AlGaAs多量子阱(MQWs)材料制备成方形微柱阵列。利用导模共振(GMR)效应,该结构激发了强烈的纵向电场分量(E_z),从而有效地满足了ISBT选择定则,增强了有源区内的吸收。在50 K温度和5 V偏压下的实验结果表明,MS-QWIP的峰值响应率达到545 mA/W,较传统的45°抛面耦合器件提升了两倍。此外,黑体响应率也提高了约1.6倍。值得注意的是,该结构还减小了光敏元的有效电学面积,从而抑制了暗电流。这项工作证明了全介质超表面能够显著提高QWIP的灵敏度和信噪比。

关键词:量子阱;半导体探测器;长波红外;介质超表面

中图分类号: O43

文献标识码: A